Ocean Engineering 267 (2023) 113269

Contents lists available at ScienceDirect

Ocean Engineering

journal homepage: www.elsevier.com/locate/oceaneng

System noise variance matrix adaptive Kalman filter method for AUV INS/DVL navigation system

Qiuying Wang [a,b,c,*], Kaiyue Liu [d], Zhongyi Cao [a,b,c]

[a] Acoustic Science and Technology Laboratory, Harbin Engineering University, Harbin, Heilongjiang, China
[b] Key Laboratory of Marine Information Acquisition and Security (Harbin Engineering University), Ministry of Industry and Information Technology, Harbin, Heilongjiang, China
[c] College of Underwater Acoustic Engineering, Harbin Engineering University, Harbin, Heilongjiang, China
[d] College of Information and Communication Engineering, Harbin Engineering University, Harbin, Heilongjiang, China

ARTICLE INFO

Keywords:
System noise variance matrix
IMU measurement Noise
INS/DVL
Frequency domain

ABSTRACT

The Inertial Navigation System (INS)/Doppler Velocity Log (DVL) navigation system is capable of locating the Autonomous Underwater Vehicle (AUV) in real-time. However, inherent errors of sensors, especially the inertial measurement unit (IMU) measurement noise changes during navigation, make the system noise variance matrix unknown and time-dependent, resulting in inaccurate Kalman filter estimates of velocity and reducing the accuracy of the navigation system. To solve this problem, this paper proposes an adaptive system noise variance matrix Kalman Filter method for AUV INS/DVL navigation system. In this method, the statistical characteristics of the IMU measurement noise are estimated by distinguishing the AUV motion information obtained by the IMU measurement and the IMU measurement noise by the frequency domain analysis method. The Kalman filter velocity estimation accuracy is improved by adaptively adjusting the system noise variance matrix based on the IMU measurement noise. Six different sets of trajectory experiments were used to validate the effectiveness and applicability of the algorithm proposed in this paper. The experimental results show that the improved KF algorithm improves the positioning accuracy by an average of 2.29‰ navigation distance compared with the traditional KF algorithm, which proves that the proposed method can improve navigation performance.

1. Introduction

Autonomous Underwater Vehicles (AUVs) are widely used in many fields of application: they are employed for ocean surveying, to carry out reconnaissance and patrol missions in the military field, to collect data on aquatic environments (Milne, 1983; Stutters et al., 2008). Regardless of the kind of mission, the vehicle is required to execute, its position must be obtained in real-time (Hwee-PinkTan et al., 2011; Paull et al., 2014). The Global Navigation Satellite System (GNSS) is unable to complete underwater positioning and provide accurate positioning information for AUV due to the fast attenuation of the radio signal as it propagates through the water (Miller et al., 2010) (see Fig. 14).

The commonly used AUVs navigation methods include geophysical field matching navigation, inertial navigation, acoustic navigation, etc. (Wang et al. 2020, 2021; Zhang et al., 2020). (1) Geophysical field matching navigation. This navigation method provides positioning information for the AUVs by matching the real-time measured physical feature information with the system's pre-stored physical field map data (Zhao et al., 2021). Therefore, geophysical field matching is highly accurate for navigation and positioning but requires establishing a geophysical field database of the operating sea area in advance, which is difficult and costly to establish a global sea area database. This method is suitable for the sea area where geophysical field databases can be easily established and cannot be used on a global scale (Thébault et al., 2015; Miller et al., 2019). (2) Inertial Navigation System (INS). INS measures the acceleration and angular velocity of the carrier in real-time by the Inertial Measurement Unit (IMU, including gyroscopes and accelerometers) and obtains the carrier position after integration (Huang, 1986). This method has the advantages of being fully autonomous and not affected by the operating environment, but its positioning error increases cumulatively with time, which greatly limits the applicability of the INS for long-endurance (Sabet et al., 2018; Narasimhappa et al., 2020). (3) Acoustic navigation. This method is a navigation method based on the Doppler effect and has the advantage that the navigation

* Corresponding author. Acoustic Science and Technology Laboratory, Harbin Engineering University, Harbin, Heilongjiang, China.
E-mail addresses: wangqiuying@hrbeu.edu.cn (Q. Wang), liukaiyue111@hrbeu.edu.cn (K. Liu), caozhongyi@hrbeu.edu.cn (Z. Cao).

https://doi.org/10.1016/j.oceaneng.2022.113269
Received 16 April 2022; Received in revised form 11 October 2022; Accepted 22 November 2022
Available online 7 December 2022
0029-8018/

error does not increase cumulatively (Morgado et al., 2013). The Doppler Velocity Log (DVL) is a commonly used acoustic velocity measurement instrument, which can measure the velocity of the carrier in real-time, but the measurement stability and accuracy are easily affected by the marine environment (Lv et al., 2020). In summary, it is difficult for a single navigation method to complete AUV positioning independently. Integrated navigation can be used to achieve complementary advantages and complete AUV positioning.

INS/DVL integrated navigation is one of the common navigation methods for AUV (Li et al., 2014; Karmozdi et al., 2020). In this navigation method, the INS error propagation equation is used as the system state equation. The DVL velocity measurement is used as the velocity reference. The velocity difference between the INS and DVL is used as the observation value. The INS error state is estimated and compensated by the Kalman filter to improve the navigation accuracy (Tang et al., 2013; Gao et al., 2015). However, the accuracy of INS/DVL integrated navigation is affected by the information fusion method, DVL velocity measurement accuracy, and INS sensor measurement accuracy.

(1) The fusion method of INS/DVL. The information fusion method can directly affect the position accuracy. Therefore, some scholars improve the navigation accuracy by improving the filtering methods, such as extended Kalman filter, unscented Kalman filter, and particle filter (Huang et al., 2010; Karras et al., 2010), etc. Luo et al. (2019) proposed a robust Kalman filter. This method models one-step forecast as Student T-Distribution and binary indicator variable as Beta Bernoulli distribution to suppress process uncertainty and measurement anomalies caused by severe maneuvers value to improve navigation accuracy. Davari and Gholami (2017) proposed an asynchronous adaptive direct Kalman filter algorithm. The algorithm adaptively adjusts the measurement noise variance matrix to improve navigation accuracy, and to solve the problem of unknown and time-dependent measurement covariance arrays. Shabani et al. (2015) proposed an asynchronous direct Kalman filtering algorithm to reduce the calculation running time, which places the prediction process in the INS loop, and the correction process is placed asynchronously outside the loop.

(2) The accuracy of DVL velocity measurement. The velocity accuracy of DVL measurements is reduced due to hydrographic environmental factors such as the underwater environment, subsea gullies, and carrier movement. The DVL velocity cannot be used as a velocity reference for the integrated navigation system, which leads to a decrease in integrated navigation accuracy (Huang et al., 2018). Zhao et al. (2016) proposed a velocity tracing method based on the constant velocity model and the assumption of slow motion of AUV for the random noise of DVL, and a fault diagnosis method based on the χ^2 rule is introduced to judge the sudden change from innovations. To deal with the outliers and observation noises in the DVL's measurements, Yao et al. (2019) used the Hybrid Interacting Multiple Model algorithm to estimate the observation noise characteristics in real-time and adaptively selected the proper models to describe the changing environment. Liu et al. (2021) proposed a two-factor robust filter combined with a chi-square test. Nortek's DVL bottom tracking data system estimated random velocity uncertainty and measured the standard deviation of instantaneous white Doppler noise (Hegrenæs et al., 2016). Then the standard deviation was inputted into the Kalman Filter of the inertial navigation system as measurement noise. To solve the problem of DVL velocity measurement error and data loss, Liu et al. (2017) established a general model of DVL measurement error caused by attitude dynamics. According to the error model, a DVL velocity correction method based on INS/DVL real-time attitude was proposed to improve the positioning accuracy of INS/DVL. Yao et al. (2020) established the velocity relationship between the transmitting beam and the receiving beam of DVL by studying the attitude and velocity data of the inertial navigation system, and the DVL velocity was corrected by the INS/DVL output attitude to improve the navigation accuracy. Lv et al. (2020) proposed an autonomous underwater vehicle navigation system based on an intelligent velocity model to improve navigation robustness. Hegrenæs and Berglund (2009) estimated the current velocity in real time and used the water velocity measured by DVL to conduct integrated navigation to improve system robustness.

(3) The measurement accuracy of inertial sensors. The INS error transfer model is used as the system state equation to complete the information fusion process in the INS/DVL navigation system. It is necessary to calibrate the INS positioning error by Kalman filter based on DVL velocity measurement since the measurement error of IMU leads to the existence of INS divergence positioning error. The INS error transfer model as the system state equation presupposes that the IMU measurement error is stable and known. That is, the statistical properties of the system state volume noise are stable(Mehra, 1972). However, during the long-term operation of AUV, the statistical characteristics of IMU measurement noise are time-varying and unknown, which directly affect the accuracy of parameter setting and positioning accuracy of the state equation model (Dong et al., 2017; Huang et al., 2018). To solve the above problems, Karmozdi et al. (2020) used the AUV motion model to improve the gyroscope output information. Then the rotation dynamics model and the improved gyroscope output information were used in the main Kalman filter to improve the navigation accuracy. In addition, to further improve the accuracy of the INS/DVL navigation system, Some scholars improved the robustness of the navigation system by introducing other sensors, such as distance sensors, pressure sensors, etc. (Lee et al., 2007; Wang et al., 2019).

In summary, most adaptive filtering methods are based on the information provided by the innovation or residual sequences that are computed in the conventional Kalman filter algorithm, on the system process noise or observation noise is adjusted. Alternatively, the positioning accuracy can be improved by adaptively adjusting the observation noise variance matrix. There are few works in the literature that analyze the IMU measurement noise from a frequency domain perspective and adjust the system noise variance matrix, for the problem that the time-varying statistical properties of IMU measurement noise affecting integrated navigation accuracy.

To solve the problem that IMU measurement accuracy affects the accuracy of INS/DVL integrated navigation, the system noise variance matrix adaptive Kalman Filter method for AUV INS/DVL navigation system is proposed in this paper. The system noise matrix is estimated and updated in real-time according to IMU measurement data. The paper is structured as follows: The second part introduces the state equation and measurement equation of INS/DVL integrated navigation and analyzes the influence of the time-varying statistical characteristics of IMU measurement noise on the positioning accuracy of the integrated navigation system; The third part analyzes the relationship between IMU measurement noise and INS system noise from the perspective of the frequency domain and revises the system noise variance matrix by using the results of IMU short-time Fourier transform to solve the problem that the Kalman filter system noise variance matrix caused by IMU noise time-varying is not suitable for positioning error. The fourth part verifies the correctness and effectiveness of the proposed algorithm through multiple sets of real ship tests. The last part summarizes the whole paper.

2. The influence analysis of IMU time-varying noise on INS/DVL integrated navigation

The INS/DVL integrated navigation obtains the INS velocity error based on the DVL velocity measurement, and then the INS navigation error is estimated and corrected by the Kalman filter to realize integrated navigation. The basic flow chart of INS/DVL integrated navigation is shown in Fig. 1. The flow chart is divided into three parts: INS navigation calculation, DVL velocity calculation, and INS/DVL information fusion.

where the superscript n represents the navigation coordinate system (east-north-up coordinate); the superscript b represents the carrier coordinate system (right-front-up coordinate); f^b、 ω_{ib}^b、 v^b represent the specific force, angular velocity, and velocity information in carrier coordinate system respectively; C_b^n represents the transformation matrix between b frame and n frame; $\widetilde{p}^n$、 $\widetilde{v}^n$、 $\widetilde{\phi}$ represent the position, velocity and attitude information calculated by INS respectively. The elements of the Kalman filter equation have the following meanings: $\widehat{X}_{k/k-1}$ represents the state one-step prediction matrix; $\boldsymbol{\Phi}_{k,k-1}$ represents the system state transition matrix; $\widehat{X}_{k-1}$ represents the state estimation matrix; $P_{k/k-1}$ represents the one-step prediction mean square error matrix; P_{k-1} represents the estimated mean square error matrix; $\boldsymbol{\Gamma}_{k-1}$ represents the system noise driving matrix; Q_k represents the system noise variance matrix; K_k represents the filter gain matrix; H_k represents the measurement matrix; R_k represents the measurement noise variance matrix; Z_k represents the measurement matrix; $\mathbf{I}$ represents the unit matrix. For more details on the INS navigation solution, please refer to the literature (Lee et al., 2007).

In addition, before INS/DVL Kalman filter information fusion, the system state equation and measurement equation need to be established, it is as follows:

$$\begin{cases} X_k = \boldsymbol{\Phi}_{k,k-1}X_{k-1} + \boldsymbol{\Gamma}_{k-1}W_{k-1} \\ Z_k = H_k X_k + V_k \end{cases} \tag{1}$$

where subscript k represents the sample time; $X = \begin{bmatrix} \delta p^T & \delta v^T & \delta\phi^T & \Delta_b{}^T & \varepsilon_b{}^T \end{bmatrix}^T$ represents the system state quantity; δp、 δv、 $\delta\phi$ represent the position error, velocity error, and misalignment angle calculated by inertial navigation respectively; Δ_b、 ε_b represents accelerometer error and gyroscope error respectively; W represents the system noise matrix; V represents the measurement noise; $Z = \widetilde{v}^n - C_b^n v^b$ represents the system observation; $H = \begin{bmatrix} \mathbf{O}_{3\times3} & \mathbf{I}_{3\times3} & [C_b^n v^b]\times & \mathbf{O}_{3\times3} & \mathbf{O}_{3\times3} \end{bmatrix}$ represents the system measurement matrix; v^b represents DVL measurement velocity; The system state transition matrix is

$$\boldsymbol{\Phi}_{k,k-1} = \begin{bmatrix} A_{pp} & A_{pv} & \mathbf{O}_{3\times3} & \mathbf{O}_{3\times3} & \mathbf{O}_{3\times3} \\ A_{vp} & A_{vv} & A_{v\phi} & C_b^n & \mathbf{O}_{3\times3} \\ A_{\phi p} & A_{\phi v} & A_{\phi\phi} & \mathbf{O}_{3\times3} & C_b^n \\ \mathbf{O}_{3\times3} & \mathbf{O}_{3\times3} & \mathbf{O}_{3\times3} & \mathbf{O}_{3\times3} & \mathbf{O}_{3\times3} \\ \mathbf{O}_{3\times3} & \mathbf{O}_{3\times3} & \mathbf{O}_{3\times3} & \mathbf{O}_{3\times3} & \mathbf{O}_{3\times3} \end{bmatrix}$$

where ,

$$A_{pp} = \begin{bmatrix} 0 & 0 & \dfrac{-v_y}{R^2} \\ \dfrac{v_x \sin\varphi}{R\cos\varphi^2} & 0 & \dfrac{-v_x\sec\varphi}{R^2} \\ 0 & 0 & 0 \end{bmatrix},$$

$$A_{vp} = \begin{bmatrix} 2\omega_{ie}\cos\varphi v_y + \dfrac{v_x v_y}{R}\sec^2\varphi & 0 & -\dfrac{v_x v_y\tan\varphi}{R^2} \\ -2\omega_{ie}v_x\cos\varphi - \dfrac{v_x^2}{R}\sec^2\varphi & 0 & \dfrac{v_x{}^2\tan\varphi}{R^2} \\ -2\omega_{ie}v_x\sin\varphi & 0 & -\dfrac{v_x{}^2 + v_y{}^2}{R^2} \end{bmatrix},$$

$$A_{pv} = \begin{bmatrix} 0 & \dfrac{1}{R} & 0 \\ \dfrac{1}{R\cos\varphi} & 0 & 0 \\ 0 & 0 & 1 \end{bmatrix},$$

$$A_{vv} = \begin{bmatrix} \dfrac{v_y\tan\varphi}{R} & 2\omega_{ie}\sin\varphi + \dfrac{v_x}{R}\tan\varphi & -\left(2\omega_{ie}\cos\varphi + \dfrac{v_x}{R}\right) \\ -2\left(\omega_{ie}\sin\varphi + \dfrac{v_x\tan\varphi}{R}\right) & -\dfrac{v_z}{R} & -\dfrac{v_y}{R} \\ 2\left(\omega_{ie}\cos\varphi + \dfrac{v_x}{R}\right) & \dfrac{2v_y}{R} & 0 \end{bmatrix},$$

$$A_{v\phi} = \begin{bmatrix} 0 & -f_z^n & f_y^n \\ f_z^n & 0 & -f_x^n \\ -f_y^n & f_x^n & 0 \end{bmatrix}, \quad A_{\phi p} = \begin{bmatrix} 0 & 0 & \dfrac{v_y}{R^2} \\ -\omega_{ie}\sin\varphi & 0 & -\dfrac{v_x}{R^2} \\ \omega_{ie}\cos\varphi + \dfrac{v_x}{R}\sec^2\varphi & 0 & -\dfrac{v_x\tan\varphi}{R^2} \end{bmatrix},$$

$$A_{\phi v} = \begin{bmatrix} 0 & -\dfrac{1}{R} & 0 \\ \dfrac{1}{R} & 0 & 0 \\ \dfrac{\tan\varphi}{R} & 0 & 0 \end{bmatrix},$$

$$A_{\phi\phi} = \begin{bmatrix} 0 & \omega_{ie}\sin\varphi + \dfrac{v_x}{R}\tan\varphi & -\left(\omega_{ie}\cos\varphi + \dfrac{v_x}{R}\right) \\ -\left(\omega_{ie}\sin\varphi + \dfrac{v_x}{R}\tan\varphi\right) & 0 & -\dfrac{v_y}{R} \\ \omega_{ie}\cos\varphi + \dfrac{v_x}{R} & \dfrac{v_y}{R} & 0 \end{bmatrix}.$$

R represents the radius of the Earth; φ represents the latitude; ω_{ie} represents the earth-rate.

According to the basic principle shown in Fig. 1, the following conclusions can be obtained:

(1) The state equation is only related to IMU measurement noise. INS navigation error iscaused by IMU measurement error. The state equation describes the transfer relationship between INS navigation errors. It can be seen that the INS navigation error transfer relationship described by the state equation is generated under

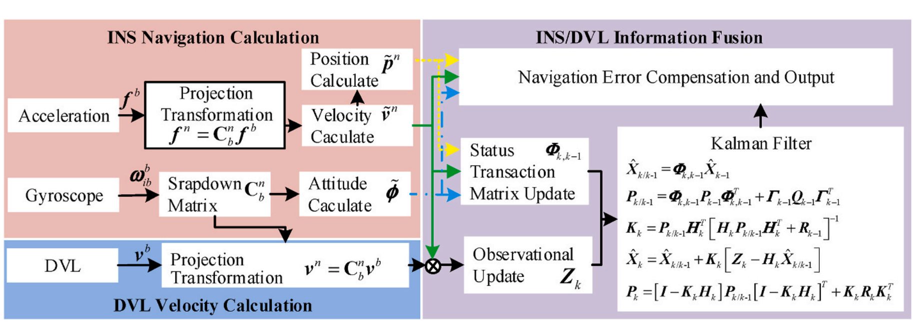

Fig. 1. Basic flow chart of INS/DVL integrated navigation.

the excitation of the initial navigation error and IMU error. According to Eq. (1), $\boldsymbol{W}_k$ describes the noise matrix of each navigation error term of the INS. According to the above analysis, the noise matrix can only be related to the statistical characteristics of IMU measurement noise. The specific expressions of $\boldsymbol{W}_k$ and $\boldsymbol{\Gamma}_{k-1}$ are derived as follows

$$\boldsymbol{W}_k = [\,\mathbf{O}_{3\times3} \quad \boldsymbol{u}_a \quad \boldsymbol{u}_g \quad \mathbf{O}_{3\times3} \quad \mathbf{O}_{3\times3}\,] \tag{2}$$

$$\boldsymbol{\Gamma}_{k-1} = \begin{bmatrix} \mathbf{O}_{3\times3} & \mathbf{O}_{3\times3} & \mathbf{O}_{3\times3} & \mathbf{O}_{3\times3} & \mathbf{O}_{3\times3} \\ \mathbf{O}_{3\times3} & \boldsymbol{C}_b^n & \mathbf{O}_{3\times3} & \mathbf{O}_{3\times3} & \mathbf{O}_{3\times3} \\ \mathbf{O}_{3\times3} & \mathbf{O}_{3\times3} & -\boldsymbol{C}_b^n & \mathbf{O}_{3\times3} & \mathbf{O}_{3\times3} \\ \mathbf{O}_{3\times3} & \mathbf{O}_{3\times3} & \mathbf{O}_{3\times3} & \mathbf{O}_{3\times3} & \mathbf{O}_{3\times3} \\ \mathbf{O}_{3\times3} & \mathbf{O}_{3\times3} & \mathbf{O}_{3\times3} & \mathbf{O}_{3\times3} & \mathbf{O}_{3\times3} \end{bmatrix} \tag{3}$$

where $\boldsymbol{u}_a$ represents the accelerometer measurement noise and $\boldsymbol{u}_w$ represents the gyroscope measurement noise.

(2) The system noise variance matrix needs to be updated in real-time based on known statistical characteristics of IMU measurement noise in the Kalman filtering. According to the basic principle of the Kalman filter, if we want to use the Kalman filter to complete information fusion, $\boldsymbol{W}_k$ must satisfy the following mathematical relationship:

$$\begin{cases} E[\boldsymbol{W}_k] = 0 \\ E\left[\boldsymbol{W}_k \boldsymbol{W}_j^T\right] = \boldsymbol{Q}_k \delta_{kj} \end{cases} \tag{4}$$

where $\boldsymbol{Q}_k$ represents the system noise variance matrix at k time.

Combining Eq. (2) and Eq. (3), the form of $\boldsymbol{Q}_k$ is obtained as:

$$\boldsymbol{Q}_k = diag(\,\mathbf{O}_{3\times3} \quad \boldsymbol{\sigma}_a^2 \quad \boldsymbol{\sigma}_g^2 \quad \mathbf{O}_{3\times3} \quad \mathbf{O}_{3\times3}\,) \tag{5}$$

where $\boldsymbol{\sigma}_a^2$ represents the measurement noise variance of the accelerometer and $\boldsymbol{\sigma}_g^2$ represents the measurement noise variance of the gyroscope.

According to the Kalman filter solution equation in Fig. 1, when the system noise variance matrix $\boldsymbol{Q}_k$ is not accurate, it will lead to the inaccurate calculation of the Kalman filter one-step prediction mean square error matrix $\boldsymbol{P}_{k/k-1}$. Thus, the filtering gain matrix $\boldsymbol{K}_k$ is inaccurate, and finally, the state estimation $\widehat{\boldsymbol{X}}_k$ is inaccurate. Therefore, to accurately set the system noise variance matrix value and estimate the system state, it is necessary to estimate the IMU measurement noise variance in real-time.

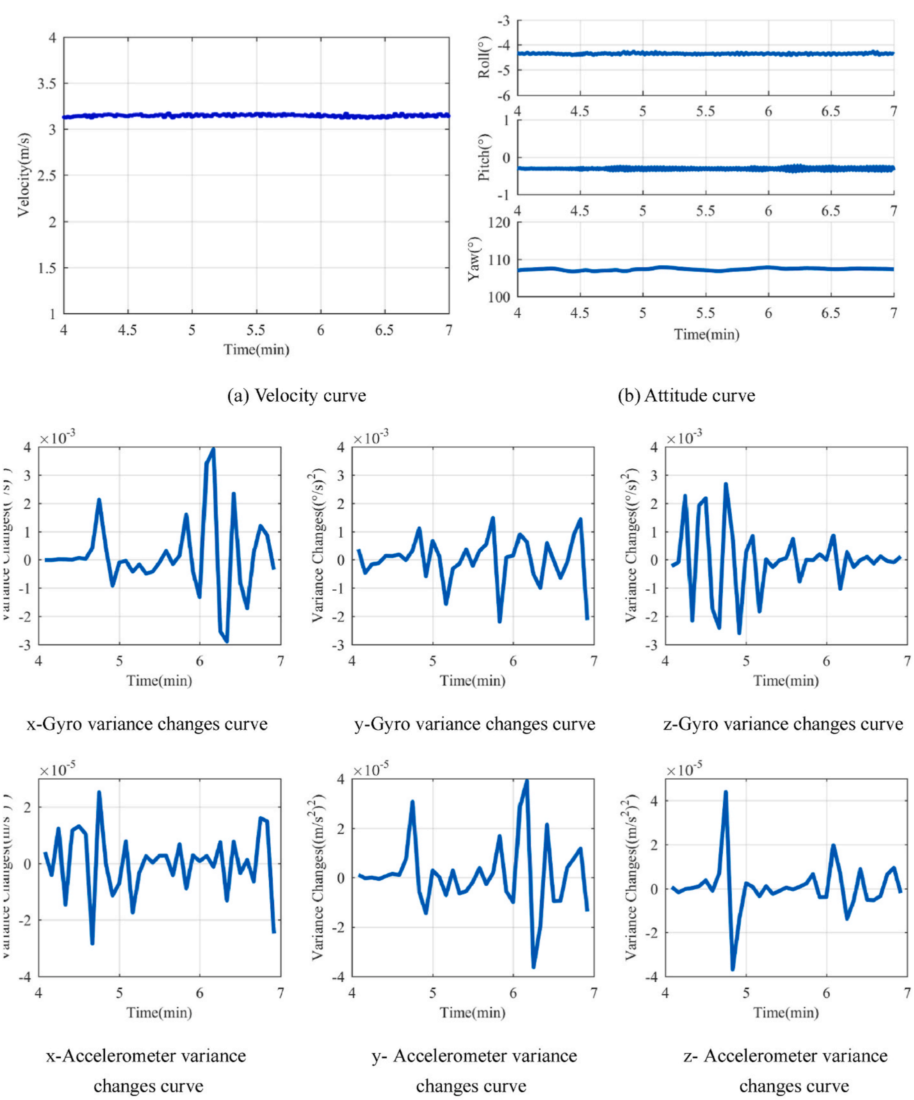

(a) Velocity curve (b) Attitude curve

x-Gyro variance changes curve y-Gyro variance changes curve z-Gyro variance changes curve

x-Accelerometer variance changes curve y- Accelerometer variance changes curve z- Accelerometer variance changes curve

(c) Statistical analysis results of IMU measurement noise

Fig. 2. IMU test results of constant speed straight line real ship test.

(3) IMU measurement noise is time-varying. Due to the limitation of AUV economic cost and installation size etc., IMU with performance between navigation level and tactical level is often selected in AUV. This type of IMU, with high short-time navigation accuracy, has large random wanderings and unstable measurement results over long periods, leading to changes in the statistical characteristics of the measurement error noise and affecting navigation accuracy (Zhao, 2014). Fig. 2 shows the results of 3-min IMU data acquisition intercepted from a ship navigation test. From the velocity curve in Fig. 2(a) and attitude curve in Fig. 2(b), it can be seen that the velocity of the carrier is stable at about 3.2 m/s in the period of 4~7min, and the attitude angle of the carrier is approximately constant. It can be approximately considered that the carrier performs uniform linear motion in this period. The mean value of IMU measurement is approximately the true value during this period. IMU measurement subtracts the mean value to obtain IMU measurement error. The statistical characteristics of the measurement error are analyzed to obtain the variation curve of IMU measurement noise variance, as shown in Fig. 2(c). It can be seen from Fig. 2(c) that the variation value of the information variance measured by the accelerometer varies between $-4\times10^{-5}\sim4.3\times10^{-5}(\mathrm{m/s^2})^2$, the variation value of the information variance measured by the gyroscope varies between $-0.003\sim0.004(\circ/\mathrm{s})^2$. This indicates that the statistical characteristics of IMU measurement noise are unstable.

The system noise variance matrix $\boldsymbol{Q}_k$ in INS/DVL navigation system is determined by the noise variance measured by IMU at the current moment. Therefore, if the statistical characteristics of the IMU measurement noise can be counted in real-time, $\boldsymbol{Q}_k$ can be set accurately. However, the IMU measurement error cannot be obtained in the navigation process, due to the real acceleration and angular velocity information of the carrier cannot be obtained in the process of AUV navigation. Therefore, it is a challenge to obtain the statistical characteristics of the IMU measurement noise during navigation and to accurately update the Kalman filter system noise variance matrix $\boldsymbol{Q}_k$, which will be discussed in the next section of the paper.

3. Adaptive system noise variance matrix kalman filtering navigation method

3.1. IMU measurement output model

The IMU measurement noise statistical characteristics parameters need to be estimated in real-time, in order to set the system noise variance matrix $\boldsymbol{Q}_k$ parameters of the Kalman filter system. However, the accurate statistical parameters of IMU measurement noise at the current measurement time cannot be obtained. In this paper, the IMU measurement information during the short time period of the k-moment preorder is used to estimate its measurement noise statistics parameters for the k-moment system noise variance matrix estimation.

In a short time (less than 10 min), IMU measurement information can be approximately considered to contain a real value, constant error, and measurement noise (Wang et al., 2019; Liu et al., 2021). The specific form is as follows:

$$\begin{cases}\boldsymbol{\omega}_g=\boldsymbol{\omega}_0+\boldsymbol{\varepsilon}_b+\boldsymbol{u}_g\\ \boldsymbol{f}_a=\boldsymbol{f}_0+\Delta_b+\boldsymbol{u}_a\end{cases}\tag{6}$$

where $\boldsymbol{\omega}_g=\begin{bmatrix}\omega_{gx} & \omega_{gy} & \omega_{gz}\end{bmatrix}^T$ represents gyroscope measurements, $\boldsymbol{\omega}_0$ represents the true angular velocity of the AUV; $\boldsymbol{f}_a=\begin{bmatrix}f_{ax} & f_{ay} & f_{az}\end{bmatrix}^T$ represents accelerometer measurements, $\boldsymbol{f}_0$ represents the true acceleration of the AUV.

3.2. Short-time fourier transform and characteristic analysis of IMU data

According to Eq. (6), IMU measurement information includes real and effective information of the carrier, constant error, and white noise. It is difficult to estimate the statistical properties of white noise directly from the IMU measurement data due to the maneuvering of the AUV motion. Spectrum analysis can transform the signal from the time domain to frequency domain, and obtain the signal strength amplitude distribution of the dynamic signal in each frequency band. It can be seen that the statistical characteristic parameters of IMU measurement noise can be estimated from the IMU frequency domain analysis results, if the frequency domain characteristics of each physical parameter in Eq. (6) are different.

3.2.1. Short Time Fourier Transform of IMU measurement data

The short-time Fourier transform (STFT) is used to analyze the spectrum of IMU measurement data. The short-time Fourier transform of IMU measurement data is defined as follows:

$$\begin{cases}X_{gi}(t,f)=\int_{-\infty}^{+\infty}\omega_{gi}(\tau)h(\tau-t)e^{-j2\pi f\tau}d\tau\\ X_{ai}(t,f)=\int_{-\infty}^{+\infty}f_{ai}(\tau)h(\tau-t)e^{-j2\pi f\tau}d\tau\end{cases}\tag{7}$$

where $i=x,y,z$ represent the uniaxial measurement output, $h(t)$ represents the window function, t represents the center point of the window function, f represents the frequency, and τ represents the time.

Therefore, the output spectrum of IMU measurement data is defined as follows:

$$\begin{cases}S_{gi}(t,f)=|X_{gi}(t,f)|^2\\ S_{ai}(t,f)=|X_{ai}(t,f)|^2\end{cases}\tag{8}$$

where $S_{gi}(t,f)$, $S_{ai}(t,f)$ represent the power spectral density of gyroscope measurement data and accelerometer measurement data respectively.

The IMU measurement data collected by a ship for a period of time are selected for STFT, and Eq. (7) is explained as follows:

(1) The IMU measurement data is multiplied by the window function $h(t)$, and the IMU measurement data is framed to obtain the short-term stable IMU measurement data, to facilitate the subsequent Fourier transform.
(2) Fourier transform is performed on the result of the intercepted signal in step 1
(3) Moving the window function on the time axis, repeating steps 1 and 2. Time resolution and frequency resolution of STFT depend on window function length and moving step length. In order to balance the accuracy of frequency analysis and time-resolved filtering, the window function length and the moving step length need to be set according to the actual situation.
(4) The Fourier transform curve obtained by the window function at different time starting points are superimposed to obtain the local time-frequency diagram of IMU measurement data.

3.2.2. Analysis of IMU frequency domain characteristics

It can be seen from Fig. 3 that the power spectral density obtained by the STFT of the original IMU measurement data has a large component around 0Hz, 25Hz, 37Hz, 73Hz, 81Hz, and 87Hz, with the largest amplitude of the power spectrum density around 0Hz. Based on Eq. (6), Eq. (8), and the results of the curve in Fig. 3, the analysis of the frequency domain characteristics of the data corresponding to each parameter of the IMU in Eq. (6) is concluded as follows:

(1) Frequency domain characteristics of carrier real motion $\boldsymbol{\omega}_0$ and $\boldsymbol{f}_0$: The AUV motion is slow compared to the on-board and

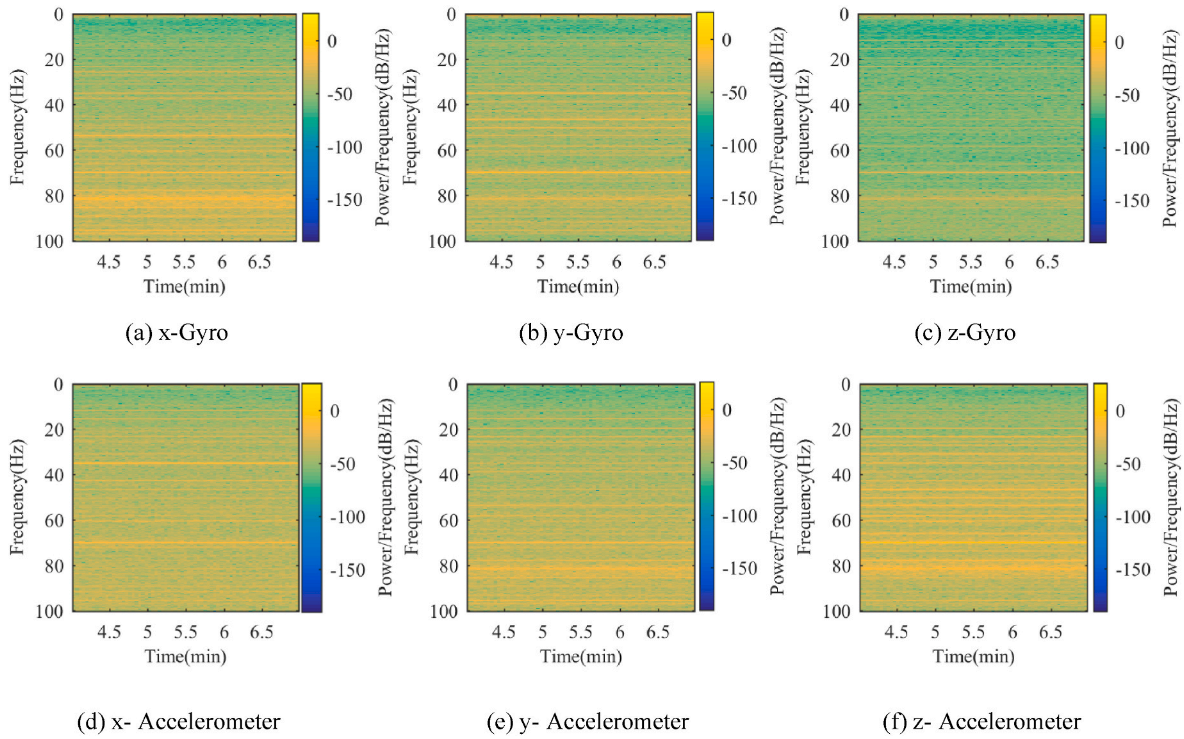

Fig. 3. The short-time Fourier change process diagram of IMU measurement data.

airborne motion. Therefore, it is approximated that the true motion components contained in the data after extraction of the IMU using a finite time window change slowly. The angular velocity and acceleration Fourier decomposition is a cumulative sum of multiple cosine components. The STFT transform results for $\boldsymbol{\omega}_0$ and $\boldsymbol{f}_0$ are evenly distributed in the frequency bands of 0Hz, 25Hz and 37Hz, and the signal intensity is high. As shown in the yellow line spectrum of the time-frequency diagram in Fig. 3.

(2) Frequency domain characteristics of constant error $\boldsymbol{\varepsilon}_b$ and Δ_b: The STFT transform results for $\boldsymbol{\varepsilon}_b$ and Δ_b are distributed around 0Hz. The 0Hz corresponding spectral line is shown in the time-frequency diagram in Fig. 3.

(3) Frequency domain characteristics of white noise $\boldsymbol{u}_a$ and $\boldsymbol{u}_g$: The STFT transform results for $\boldsymbol{u}_a$ and $\boldsymbol{u}_\omega$ should be distributed in the whole frequency band, and the signal strength is low. It can be seen from Fig. 3 that the green part of the time-frequency diagram is background noise.

In summary, the frequency domain characteristics of real motion ($\boldsymbol{\omega}_0$, $\boldsymbol{f}_0$), constant error ($\boldsymbol{\varepsilon}_b$, Δ_b), white noise ($\boldsymbol{u}_a$, $\boldsymbol{u}_g$) are regular high strength, zero-band high strength, and full-band low strength. Therefore, if the white noise magnitude in the power spectrum can be determined, the system noise variance matrix $\boldsymbol{Q}_k$ parameter can be determined. If the full-band low-intensity white noise component can be separated from the STFT result of the IMU measurement data, the statistical characteristics of the noise measured by the IMU can be obtained, which is the focus of discussion in the next section.

3.3. System noise variance matrix Q_k parameter estimation

3.3.1. Distribution probability statistics of IMU STFT signal strength

After the STFT transform of the IMU measurement data, the signal power $\{\overline{S}_{gj}\}$ $(j = 1, 2, \cdots, N)$ of the IMU measurement data in different frequency bands is obtained. On this basis, the distribution probability of signal power $\overline{S}_{gj}$ is calculated. The distribution probability is defined as follows in this paper. The probability that $\forall \overline{S}_{gj} \in [\min(\overline{S}_g), \overline{S}_{g0}]$ in all signal powers $\{\overline{S}_{gj}\}$ is $P(\overline{S}_g < \overline{S}_{g0})$, calculated as follows:

$$P(\overline{S}_g < \overline{S}_{g0}) = \frac{N_{\overline{S}_g < \overline{S}_{g0}}}{N} \tag{9}$$

where N represents the total number of discrete points of signal power obtained by short-time Fourier transform, $N_{\overline{S}_g < \overline{S}_{g0}}$ represents the number of signal power less than $\overline{S}_{g0}$.

Combining the conclusions of Section 3.2 and Fig. 3, it can be seen that the frequency domain characteristics of the AUV true motion information are high in intensity but low in the number of discrete points of signal intensity. Conversely, the IMU white noise frequency domain characteristics are low in intensity but high in the number of signal intensity discrete points. The value range of $\overline{S}_{g0}$ is $-140dB \sim 0dB$. Therefore, the closer the value of $\overline{S}_{g0}$ is to -140dB, the smaller the value of $P(\overline{S}_g < \overline{S}_{g0})$. Conversely, the closer the value of $\overline{S}_{g0}$ is to 0 dB, the larger the value of $P(\overline{S}_g < \overline{S}_{g0})$. According to Eq. (10), the signal strength distribution probability $P(\overline{S}_a < \overline{S}_{a0})$ of the accelerometer is obtained.

Based on the results of IMU STFT signal intensity distribution probability $P(\overline{S}_g < \overline{S}_{g0})$ and $P(\overline{S}_a < \overline{S}_{a0})$, the "segmented data point" between the frequency domain intensity of the AUV motion information and the frequency domain intensity of the white noise in the IMU measurement data are determined. The calculation formula is as follows:

$$\begin{cases} P(\overline{S}_g < \overline{S}_{g0}) \geq p_g \\ P(\overline{S}_a < \overline{S}_{a0}) \geq p_a \end{cases} \tag{10}$$

where p_g, p_a represent probability threshold of gyroscope measurement data and accelerometer measurement data, respectively. $P(\overline{S}_i < \overline{S}_{i0}) \geq p_i$ represents that when the signal power distribution function is greater than or equal to p_i, the signal power amplitude is less than $\overline{S}_{i0}$. According to this, the signal power threshold $\overline{S}_{g0}$ and $\overline{S}_{a0}$ for distinguishing white noise and AUV motion information are obtained.

3.3.2. Frequency component separation of carrier motion based on IMU STFT

The signal power $\{\overline{S}_{gj}\}$, $\{\overline{S}_{aj}\}$ $(j = 1, 2, \cdots, N)$ of the IMU measurement signal in different frequency bands obtained by Eq. (8) is compared with the signal power thresholds $\overline{S}_{g0}$ and $\overline{S}_{a0}$ obtained by Eq. (10). The signal intensity above the threshold is removed to obtain the new spectrum $\overline{S}_{\omega}^{new}$ and $\overline{S}_{a}^{new}$. The calculation formula is as follows:

$$\begin{cases} \overline{S}_{gk}^{new} = \overline{S}_{gj}, \overline{S}_{gj} > \overline{S}_{g0} \\ \overline{S}_{ak}^{new} = \overline{S}_{aj}, \overline{S}_{aj} > \overline{S}_{a0} \end{cases} \tag{11}$$

where $\overline{S}_{gk}^{new}$ represents the element in $\overline{S}_{g}^{new}$; $\overline{S}_{ak}^{new}$ represents the element in $\overline{S}_{a}^{new}$.

3.3.3. Parameter estimation of IMU white noise statistical characteristics

The IMU output spectrum is eliminated according to the threshold value to obtain the new spectrum $\overline{S}_{g}^{new}$ and $\overline{S}_{a}^{new}$. $\overline{S}_{g}^{new}$ and $\overline{S}_{a}^{new}$ can be approximated as a white noise spectrum. According to the relationship between power spectrum and white noise variance, the white noise variance is calculated as follows:

$$\begin{cases} \sigma_g = \sqrt{10^{\frac{\left|\overline{S}_{g}^{new}\right|}{10}}} \\ \sigma_a = \sqrt{10^{\frac{\left|\overline{S}_{a}^{new}\right|}{10}}} \end{cases} \tag{12}$$

where $\left|\overline{S}_{g}^{new}\right|$, $\left|\overline{S}_{a}^{new}\right|$ represent the mean value of the power spectrum amplitude of $\overline{S}_{g}^{new}$ and $\overline{S}_{a}^{new}$, respectively; σ_g represents gyroscope white noise variance, and σ_a represents accelerometer white noise variance. The system noise variance is adjusted according to the relationship between the system noise variance and IMU white noise variance in Eq. (2).

In addition, frequent adjustment of $\boldsymbol{Q}_k$ can destroy the stability of the convergence process of the filtered state volume estimation, although the Kalman filter system noise variance matrix $\boldsymbol{Q}_k$ describes the noise characteristics of the system at the current moment k of the filter. Therefore, the judgment condition for the adjustment of $\boldsymbol{Q}_k$ in the filtering process is as follows:

$$\begin{cases} \sigma_{g_{k+1}} - \sigma_{g_k} \geq \delta\sigma_{g_0} \\ \sigma_{a_{k+1}} - \sigma_{a_k} \geq \delta\sigma_{a_0} \end{cases} \tag{13}$$

where σ_{g_k} represents gyroscope white noise variance at time k; σ_{a_k} represents accelerometer white noise variance at time k; $\delta\sigma_{g_0}$ and $\delta\sigma_{a_0}$ represent the adjustment threshold of $\boldsymbol{Q}_k$.

The Kalman filter system noise variance matrix $\boldsymbol{Q}_k$ is adjusted when the results of the IMU spectral characteristics analysis satisfy Eq. (13).

The basic flow chart of the system noise variance matrix $\boldsymbol{Q}_k$ adaptive Kalman Filter method for AUV INS/DVL navigation system is shown in Fig. 4.

4. Experimental results and analysis

A ship test was used for validation, in order to verify the correctness and effectiveness of the system noise variance matrix $\boldsymbol{Q}_k$ adaptive Kalman Filter method for AUV INS/DVL navigation system proposed in this paper.

4.1. Overview of the experiment

4.1.1. Test sensor configuration

The test equipment includes INS, DVL, and GPS. Among them, INS and DVL are used to complete the integrated navigation algorithm in this paper, and GPS is used as the position reference information to evaluate the integrated navigation accuracy. The installation relationship of each piece of equipment on the ship is shown in Fig. 5. The sensor performance indicators are shown in Table 1. The INS is fixedly installed on the transfer rigid plate, and then the rigid plate is fixed on the ship deck by welding points. The DVL is rigidly suspended on the side of the

Fig. 5. Test sensor installation structure.

Table 1
Sensor performance indicators.

sensor		Indicator	Parameter	Data update frequency
INS	Gyroscope	Constant drift	0.01°/h	200Hz
		Random noise	0.005 ∘/$\sqrt{h}$	
	Accelerometer	Constant drift	50 μg	
GPS		Measurement accuracy	1.8m (RMS)	1Hz
DVL		Measurement accuracy	0.5%	1Hz

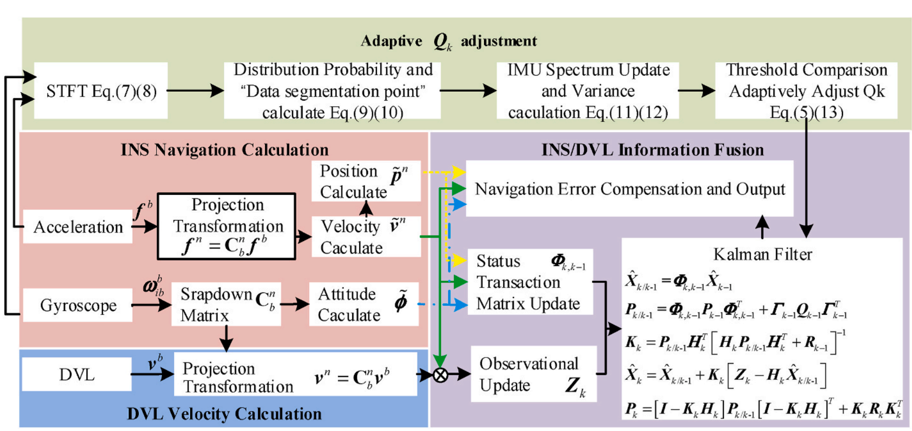

Fig. 4. Flow chart of the system noise variance matrix $\boldsymbol{Q}_k$ adaptive Kalman Filter method for INS/DVL navigation.

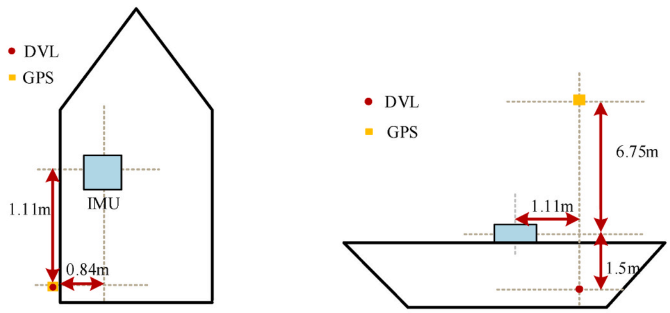

(a) Vertical viewport (b) Left viewport

Fig. 6. Test equipment lever arm measurement results.

boat by the tripod. The GPS receiving antenna is mounted on the top of the Doppler log tripod.

4.1.2. Ship test

The space of each sensor is not uniform, affected by the installation. Test the mounting lever arm between each sensor and the installation deviation angle between INS and DVL. The lever arm measurement results of the test equipment are shown in Fig. 6. Taking the inertial sensor as the center point, the lever arm of GPS is $[0.84\text{m} \quad 1.11\text{m} \quad 6.75\text{m}]$. The lever arm of DVL is $[0.84\text{m} \quad 1.11\text{m} \quad 1.5\text{m}]$. The installation deviation angle of pitch angle between INS and DVL is -0.2129°, and the installation deviation angle of heading angle is -2.7312°. During the experiment, the test ship sails freely for 25 min to complete the initial alignment and then starts the integrated navigation.

4.1.3. Accuracy evaluation method

Firstly, the difference between GPS position measurement reference and INS/DVL integrated navigation position is used to evaluate the accuracy of integrated navigation. Secondly, the unimproved Kalman filter is used to compare with the improved Kalman filter proposed in this paper as INS/DVL integrated navigation method to verify the effectiveness of this method. Finally, in order to verify the applicability of the proposed method, multiple voyages are used for verification.

4.1.4. Parameter setting of improved filtering method

The initial setting of the Kalman filter is:

$$\begin{aligned}
\boldsymbol{P_0} = diag\big([&1.57\times10^{-6}(\text{rad}) \;\; 1.57\times10^{-6}(\text{rad}) \;\; 1.57\times10^{-6}(\text{m}) \;\; 0.1(\text{m/s}) \;\; 0.1(\text{m/s}) \;\; 0.1(\text{m/s}) \;\; 4.85\times10^{-4}(\text{rad}) \;\; 4.85\times10^{-4}(\text{rad}) \;\; 4.85\times10^{-4}(\text{rad}) \\
&9.8\times10^{-4}(\text{m/s}^2) \;\; 9.8\times10^{-4}(\text{m/s}^2) \;\; 9.8\times10^{-4}(\text{m/s}^2) \;\; 1.45\times10^{-7}(\text{rad/s}) \;\; 1.45\times10^{-7}(\text{rad/s}) \;\; 1.45\times10^{-7}(\text{rad/s})]\big)^2 \\
\boldsymbol{Q_0} = diag\big([&0 \;\; 0 \;\; 0 \;\; 0.01(\text{m/s}^2) \;\; 0.2(\text{m/s}^2) \;\; 0.01(\text{m/s}^2) \;\; 4.85\times10^{-8}(\text{rad/s}) \;\; 4.85\times10^{-8}(\text{rad/s}) \;\; 4.85\times10^{-8}(\text{rad/s}) \;\; 0 \;\; 0 \;\; 0 \;\; 0 \;\; 0 \;\; 0]\big)^2 \\
\boldsymbol{R}_0 = diag(&[0.01(\text{m/s}) \;\; 0.01(\text{m/s}) \;\; 0.01(\text{m/s})])^2
\end{aligned}$$

In Eq. (7), the length of STFT is 1024 sampling points, the window

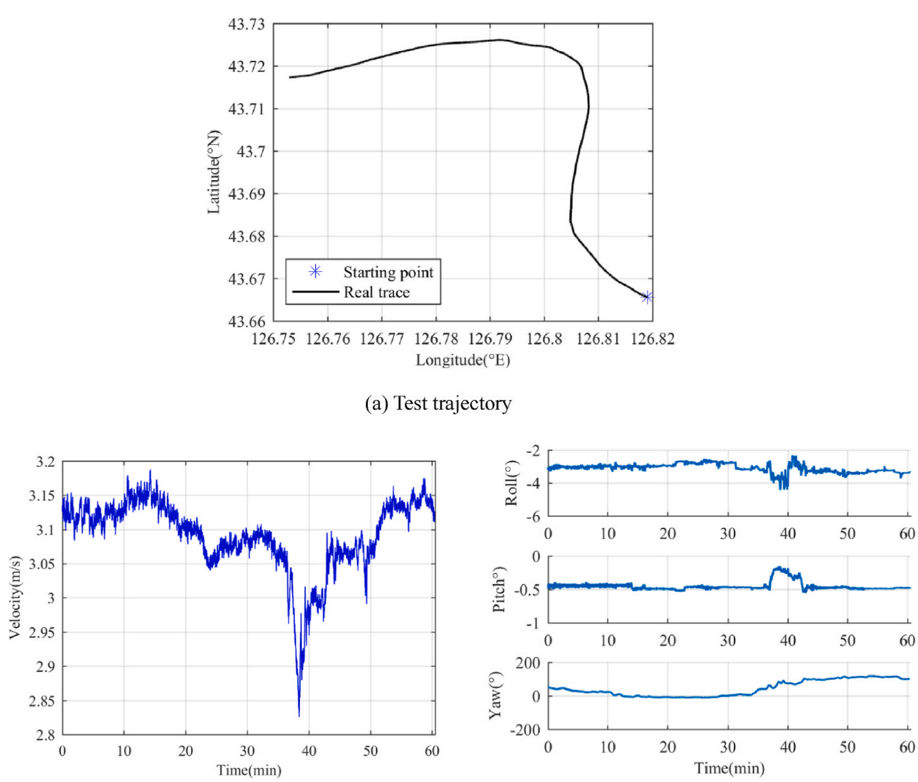

(a) Test trajectory

(b) Test velocity (c) Test attitude

Fig. 7. Experimental navigation trajectory, velocity, and attitude.

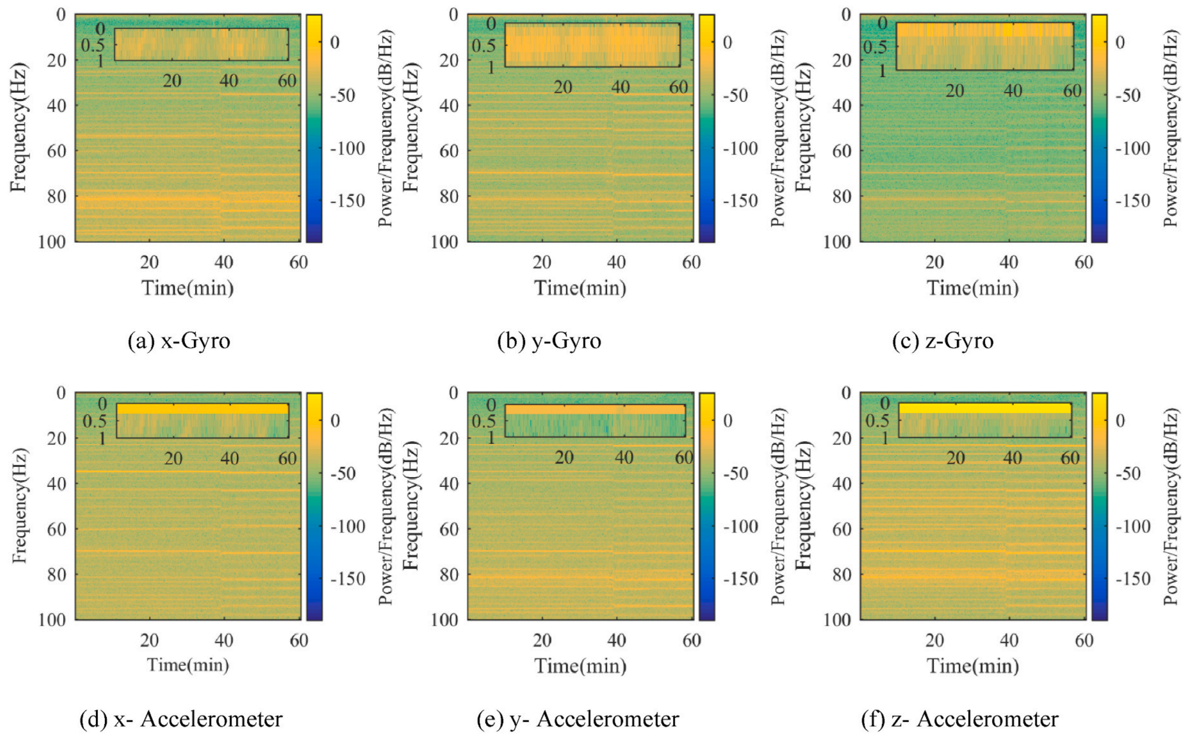

Fig. 8. Short Time Fourier Transform of IMU Measurement data.

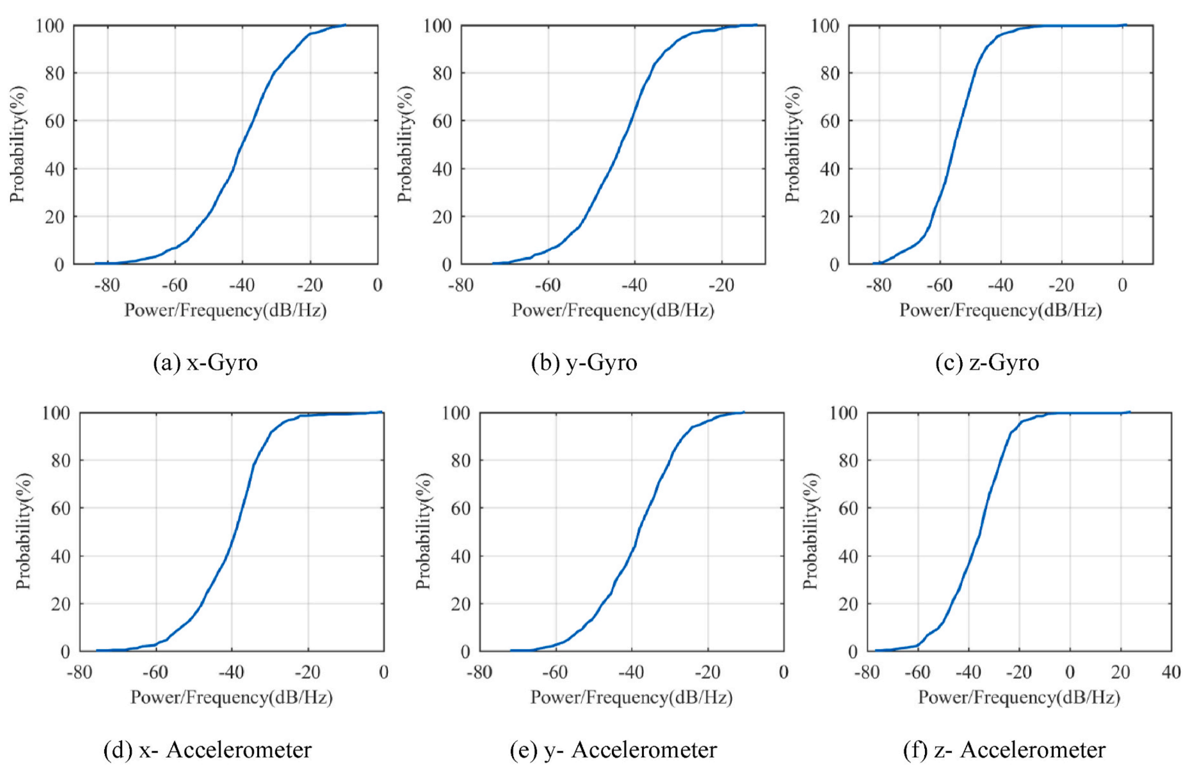

Fig. 9. Signal strength probability distribution curve.

function is Hamming window, the length of the window function is 1024 sampling points, and the moving step is 512 sampling points. The probability thresholds in Eq. (10) are 0.9 and 0.85 respectively. The judgment threshold in Eq. (13) are 3.25×10^{-7}°/s and $3.85\times 10^{-4}\mathrm{m/s^2}$ respectively.

4.2. Parameter characteristic analysis of single flight

In this section, data from one voyage is chosen to analyze each parameter in detail. The test trajectory, velocity, and attitude are shown in Fig. 7. The voyage time is about 60 min and the average speed is about 3 m/s. The test ship turns in 10–15 min and 32–36 min and has velocity

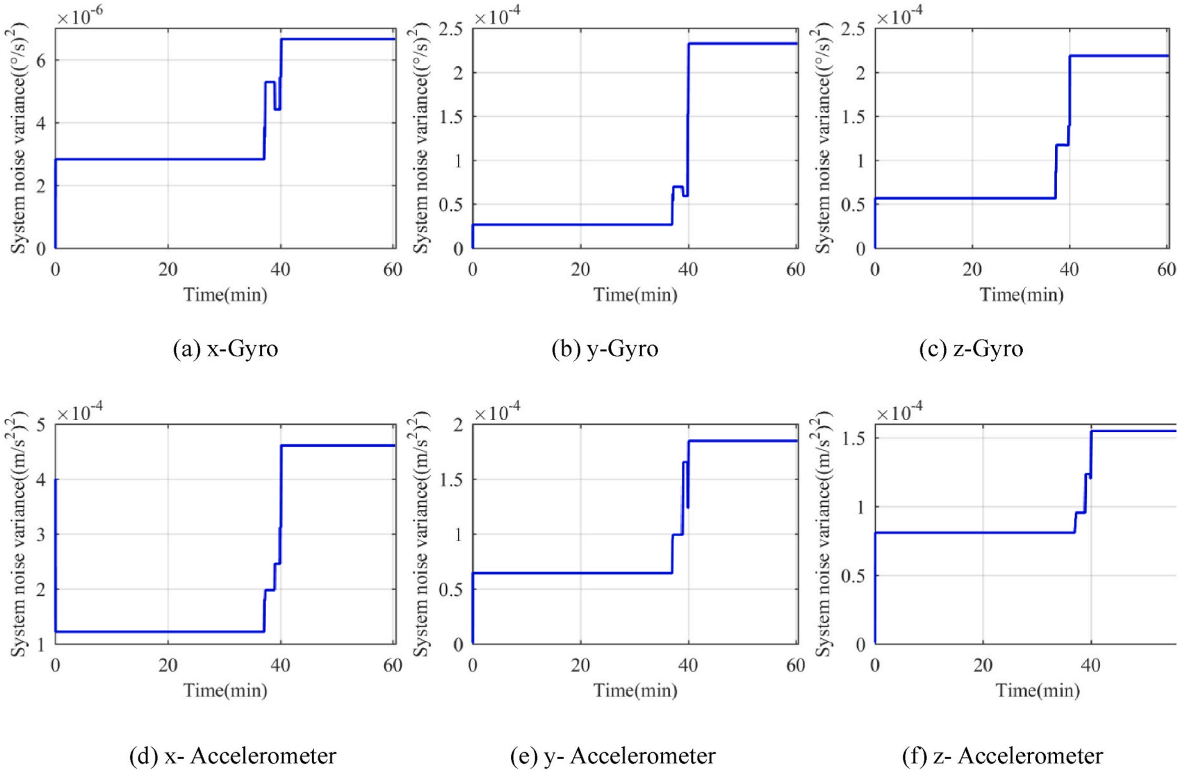

Fig. 10. System noise variance matrix Q_k adjustment curve.

adjustment in 36–39 min.

Fig. 8 is the Short-Time Fourier Transform results of IMU axis measurement information. Fig. 9 is the probability distribution curve of the IMU axis output data signal strength. Fig. 10 is the system noise variance matrix Q_k adjustment diagram in the process of integrated navigation.

It can be seen from Fig. 8 that the AUV motion information measured in each axis is mainly focused on fixed frequencies. The signal strength of each axis is stronger at 0Hz, especially the measured value of the accelerometer because the accelerometer can measure the earth's gravity acceleration. In the figure, the yellow-green color below −60 dB of low signal intensity is distributed in the whole time-frequency diagram, indicating the white noise measured by IMU.

It can be seen from Fig. 9 that the lower the signal strength, the signal strength probability distribution function value is close to 0, and the greater the signal strength, the closer the signal strength probability distribution function is to 1. When the signal strength is greater than-20dB, the growth rate of the probability distribution function is relatively reduced, which shows that the signal strength of the IMU Fourier transform is greater than-20dB at a certain time. This means that the frequency domain characteristics of IMU white noise and useful information are different. The probability of low white noise signal strength is high, and the probability of high useful information signal strength is low. Therefore, the "data segmentation point" can be obtained by comparing it with the probability threshold.

It can be seen in Fig. 10 that the Q-matrix parameter corresponding to the x-axis gyroscope has 7 corrections, the Q-matrix parameter corresponding to the y-axis gyroscope has 7 corrections, and the Q-matrix parameter corresponding to the z-axis gyroscope has 5 corrections. The Q-matrix parameter corresponding to the x-axis accelerometer has 5 corrections, The Q-matrix parameter corresponding to the y-axis accelerometer has 6, and the Q-matrix parameter corresponding to the z-axis accelerometer has 5 corrections.

The average value of east velocity error of unimproved Kalman filter and improved Kalman filter is -0.0119m/s and -0.0085m/s. The average value of north velocity error of unimproved Kalman filter and improved Kalman filter is -0.2066m/s and -0.2046m/s. The mean value of improved Kalman filter velocity error is less than that of improved Kalman filter velocity error, which indicates that the accuracy of

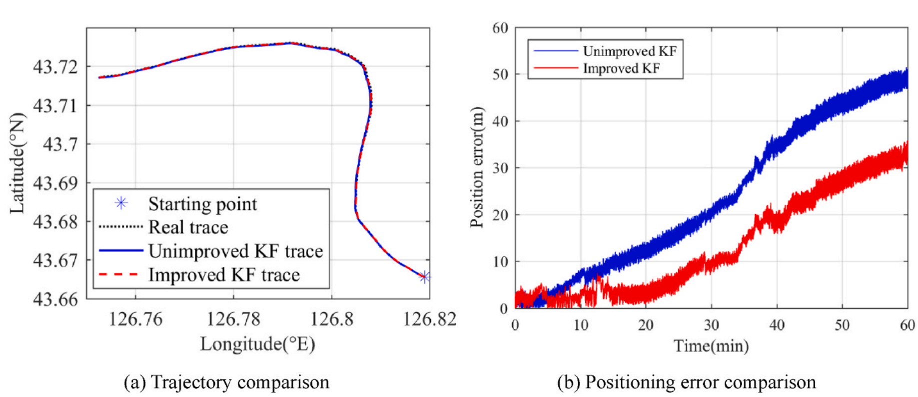

Fig. 11. Integrated navigation positioning results.

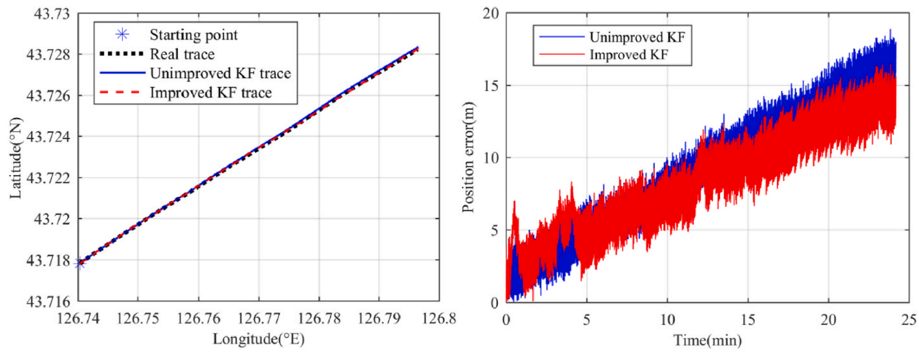

(a) Trajectory comparison (b) Positioning error comparison

Fig. 12. Test 1 Navigation and positioning results.

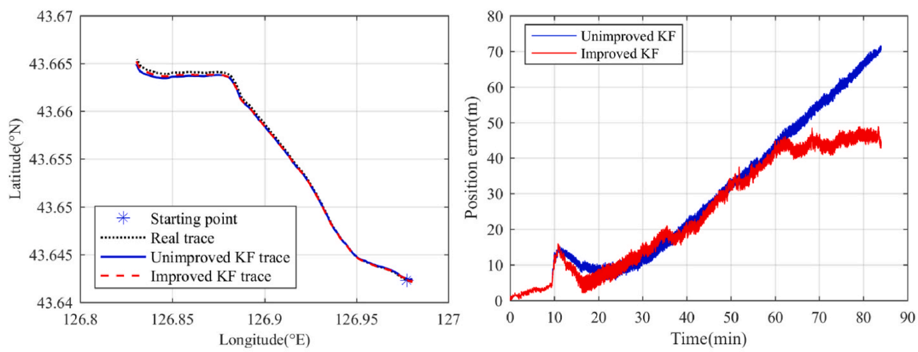

(a) Trajectory comparison (b) Positioning error comparison

Fig. 13. Test 2 Navigation and positioning results.

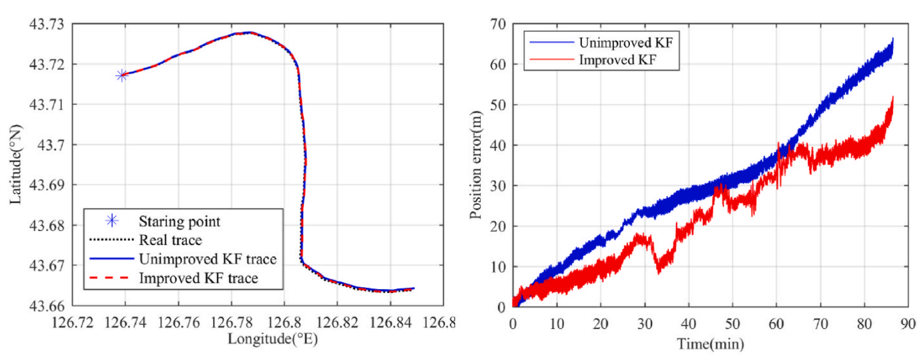

(a) Trajectory comparison (b) Positioning error comparison

Fig. 14. Test 3 Navigation and positioning results.

improved Kalman filter velocity is improved.The integrated navigation results are shown in Fig. 11. It can be seen from the figure that the final positioning error obtained by the improved Kalman filter is 36.15m, and the final positioning accuracy is 2.67‰ navigation distance. The final positioning error obtained by the unimproved Kalman filter algorithm is 51.36m, and the final positioning accuracy is 3.80‰ navigation distance. The positioning error is reduced by 15.21m and the positioning accuracy is improved by 1.13‰ navigation distance.

4.3. The applicability verification of the multi-flight method

To verify the applicability of the proposed method, five experiments are carried out under the same experimental conditions. The results of integrated navigation and positioning are shown in Figs. 12–16. Table 2 shows the comparison of the navigation results of the five groups of experiments. The navigation accuracy is defined as the percentage of the positioning error to the navigation distance. Therefore, the average navigation accuracy of the improved Kalman filter method is 2.29‰ navigation distance, and the average accuracy is increased by 1.4‰ navigation distance. The maximum accuracy improvement percentage is 2.45‰ navigation distance, and the minimum is 0.37‰ navigation distance. Through five groups of experiments on different tracks, it can be seen that compared with the unmodified Kalman filter algorithm, the positioning accuracy of the proposed algorithm is improved, and the effectiveness of the proposed algorithm is proved.

5. Conclusion

This paper proposes an improved INS/DVL integrated navigation method based on the system noise variance matrix adaptive Kalman

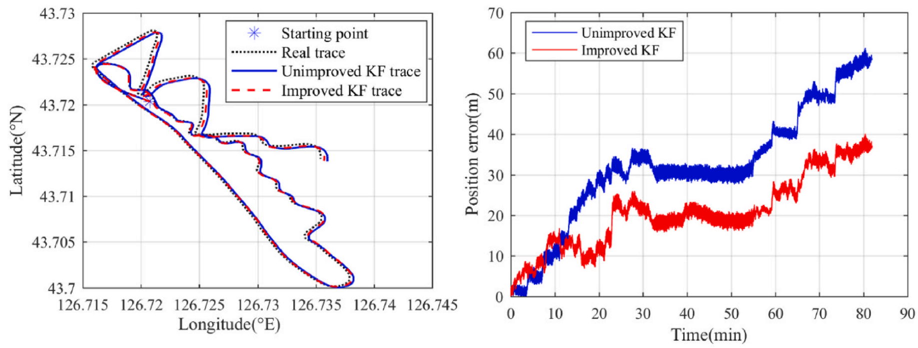

(a) Trajectory comparison (b) Positioning error comparison

Fig. 15. Test 4 Navigation and positioning results.

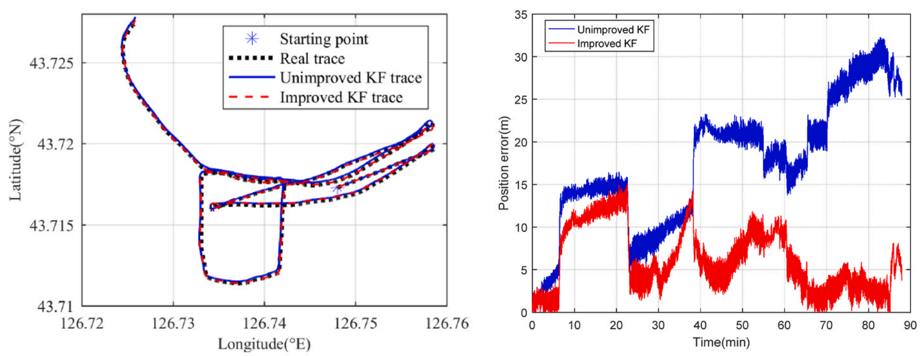

(a) Trajectory comparison (b) Positioning error comparison

Fig. 16. Test 5 Navigation and positioning results.

Table 2
The precise comparison of the two algorithms.

	Navigation distance (km)	navigation time (min)	Unimproved Kalman filter positioning error (m)	Improved Kalman filter positioning error (m)	Accuracy improvement percentage (‰D)
Test 1	6.40	24.18	17.99	15.62	0.37
Test 2	13.40	84	71.54	38.66	2.45
Test 3	16.71	86.52	65.40	50.71	0.88
Test 4	13.29	82	58.73	37.18	1.62
Test 5	12.94	88	25.60	3.86	1.68

Filter, which is used to solve the problem of INS/DVL positioning accuracy reduction caused by the change of inertial sensor measurement noise with time. In this method, the spectral information from the IMU measurement data is used for navigation. Firstly, the INS system noise is only related to the IMU measurement noise from the frequency domain perspective, and the IMU measurement noise changes with time. Secondly, the frequency domain information of the IMU measurement data in the short time period before the k moment is used to estimate the IMU measurement noise statistical parameters, due to the different frequency domain characteristics corresponding to each physical parameter of the IMU measurement information respectively. The system noise variance matrix at moment k is estimated from the IMU measurement noise statistical parameters. Finally, the proposed algorithm is validated by several sets of on-lake experiments with different trajectories. The experimental results show that the proposed algorithm can estimate the IMU measurement noise and correct the system noise variance matrix to improve the positioning accuracy of integrated navigation, though the positioning error is not significantly improved in the straight track. The average navigation accuracy of the improved Kalman filter method is 2.29‰ navigation distance, which indicates that the proposed algorithm has better accuracy when the system noise changes.

CRediT authorship contribution statement

Qiuying Wang: Conceptualization, Supervision, Funding acquisition. **Kaiyue Liu:** Methodology, Formal analysis, Writing – original draft, Writing – review & editing. **Zhongyi Cao:** Investigation.

Declaration of competing interest

The authors declare the following financial interests/personal relationships which may be considered as potential competing interests: Qiuying Wang reports financial support was provided by National Natural Science Foundation of China. Qiuying Wang reports financial

support was provided by Natural Science Foundation of Heilongjiang Province, China.

Data availability

The authors do not have permission to share data.

Acknowledgment

This work was supported by the National Natural Science Foundation of China (No.51879046); and the Natural Science Foundation of Heilongjiang Province of China (No.YQ2019F001).

References

Davari, N., Gholami, A., 2017. An asynchronous adaptive direct kalman filter algorithm to improve underwater navigation system performance. IEEE Sensor. J. 17 (4), 1061–1068. https://doi.org/10.1109/JSEN.2016.2637402.

Dong, P., Jing, Z., Leung, H., Shen, K., 2017. Variational bayesian adaptive cubature information filter based on wishart distribution. IEEE Trans. Automat. Control 62 (11), 6051–6057. https://doi.org/10.1109/TAC.2017.2704442.

Gao, W., Li, J., Zhou, G., Li, Q., 2015. Adaptive kalman filtering with recursive noise estimator for integrated SINS/DVL systems. J. Navig. 68 (1), 142–161. https://doi.org/10.1017/S0373463314000484.

Hegrenæs, Ø., Berglund, E., 2009. Doppler water-track aided inertial navigation for autonomous underwater vehicle. Oceans 1–10, 2009.

Hegrenæs, Ø., Ramstad, A., Pedersen, T., Velasco, D., 2016. Validation of a New Generation DVL for Underwater Vehicle Navigation, 2016. IEEE/OES Autonomous Underwater Vehicles (AUV), Tokyo, Japan, pp. 342–348.

Huang, d., 1986. Inertial Navigation System. National Defense Industry Press.

Huang, L., He, B., Zhang, T., 2010. An autonomous navigation algorithm for underwater vehicles based on inertial measurement units and sonar. Wuhan. In: 2010 2nd International Asia Conference on Informatics in Control, Automation and Robotics (CAR 2010), pp. 311–314.

Huang, Y., Zhang, Y., Wu, Z., Li, N., Chambers, J., 2018. A novel adaptive kalman filter with inaccurate process and measurement noise covariance matrices. IEEE Trans. Automat. Control 63 (2), 594–601. https://doi.org/10.1109/TAC.2017.2730480.

Tan, Hwee-Pink, Diamant, Roee, Seah, W.K.G., Waldmeyer, Marc, 2011. A survey of techniques and challenges in underwater localization. Ocean Eng. 38 (14–15), 1663–1676. https://doi.org/10.1016/j.oceaneng.2011.07.017.

Karmozdi, A., Hashemi, M., Salarieh, H., Alasty, A., 2020. INS-DVL navigation improvement using rotational motion dynamic model of AUV. IEEE Sensor. J. 20 (23), 14329–14336. https://doi.org/10.1109/JSEN.2020.3007929.

Karras, G.C., Loizou, S.G., Kyriakopoulos, K.J., 2010. On-line State and Parameter Estimation of an Under-actuated Underwater Vehicle Using a Modified Dual Unscented Kalman Filter, 2010. IEEE/RSJ International Conference on Intelligent Robots and Systems, Taipei, Taiwan, pp. 4868–4873.

Lee, P.-M., Jun, B.-H., Kim, K., Lee, J., 2007. Simulation of an inertial acoustic navigation system with range aiding for an autonomous underwater vehicle. IEEE J. Ocean. Eng. 32 (2), 327–345. https://doi.org/10.1109/JOE.2006.880585.

Li, W., Wu, W., Wang, J., Wu, M., 2014. A novel backtracking navigation scheme for Autonomous Underwater Vehicles. Measurement 47, 496–504. https://doi.org/10.1016/j.measurement.2013.09.022.

Liu, P., Wang, B., Deng, Z., Fu, M., 2017. A correction method for DVL measurement errors by attitude dynamics. IEEE Sensor. J. 17 (14), 4628–4638. https://doi.org/10.1109/JSEN.2017.2712282.

Liu, S., Zhang, T., Zhang, J., Zhu, Y., 2021. A new coupled method of SINS/DVL integrated navigation based on improved dual adaptive factors. IEEE Trans. Instrum. Meas. 70, 1–11. https://doi.org/10.1109/TIM.2021.3106118.

Luo, L., Zhang, Y., Fang, T., Li, N., 2019. A new robust kalman filter for SINS/DVL integrated navigation system. IEEE Access 7, 51386–51395. https://doi.org/10.1109/ACCESS.2019.2911110.

Lv, P.-F., He, B., Guo, J., Shen, Y., Yan, T.-H., Sha, Q.-X., 2020. Underwater navigation methodology based on intelligent velocity model for standard AUV. Ocean Eng. 202 https://doi.org/10.1016/j.oceaneng.2020.107073.

Mehra, R.K., 1972. Approaches to adaptive filtering. Automatic Control IEEE Transactions on 17 (5), 693–698. https://doi.org/10.1109/TAC.1972.1100100.

Miller, A., Miller, B., Miller, G., 2019. AUV Position Estimation via Acoustic Seabed Profile Measurements, 2018. IEEE/OES Autonomous Underwater Vehicle Workshop (AUV), pp. 1–5.

Miller, P.A., Farrell, J.A., Zhao, Y., Djapic, V., 2010. Autonomous underwater vehicle navigation. IEEE J. Ocean. Eng. 35 (3), 663–678. https://doi.org/10.1109/JOE.2010.2052691.

Milne, P., 1983. Underwater Acoustic Positioning Systems. Gulf Publishing Co Houston Tx.

Morgado, M., Oliveira, P., Silvestre, C., 2013. Tightly coupled ultrashort baseline and inertial navigation system for underwater vehicles: an experimental validation. J. Field Robot. 30 (1), 142–170. https://doi.org/10.1002/rob.21442.

Narasimhappa, M., Mahindrakar, A.D., Guizilini, V.C., Terra, M.H., Sabat, S.L., 2020. MEMS-based IMU drift minimization: sage husa adaptive robust kalman filtering. IEEE Sensor. J. 20 (1), 250–260. https://doi.org/10.1109/JSEN.2019.2941273.

Paull, L., Saeedi, S., Seto, M., Li, H., 2014. AUV navigation and localization: a review. IEEE J. Ocean. Eng. 39 (1), 131–149. https://doi.org/10.1109/JOE.2013.2278891.

Sabet, M.T., Daniali, H.M., Fathi, A., Alizadeh, E., 2018. A low-cost dead reckoning navigation system for an AUV using a robust AHRS: design and experimental analysis. IEEE J. Ocean. Eng. 43 (4), 927–939. https://doi.org/10.1109/JOE.2017.2769838.

Shabani, M., Davari, A.G.N., Dynamics, N., 2015. Asynchronous direct Kalman filtering approach for underwater integrated navigation system. Nonlinear Dynam. 80 (1–2), 71–85. https://doi.org/10.1007/s11071-014-1852-9.

Stutters, L., Liu, H., Tiltman, C., Brown, D.J., 2008. Navigation technologies for autonomous underwater vehicles. IEEE Transactions on Systems, Man, and Cybernetics, Part C (Applications and Reviews) 38 (4), 581–589. https://doi.org/10.1109/TSMCC.2008.919147.

Tang, K., Wang, J., Li, W., Wu, W., 2013. A novel INS and Doppler sensors calibration method for long range underwater vehicle navigation. Sensors 13 (11), 14583–14600. https://doi.org/10.3390/s131114583.

Thébault, E., Finlay, C.C., Alken, P., Beggan, C.D., Canet, E., Chulliat, A., Langlais, B., Lesur, V., Lowes, F.J., Manoj, C., Schachtschneider, M.R.R., 2015. Evaluation of candidate geomagnetic field models for IGRF-12. Earth Planets Space 67. https://doi.org/10.1186/s40623-015-0273-4.

Wang, C., Wang, B., Deng, Z., Fu, M., 2021. A Matching Algorithm with Gravity Field Matching Characteristic for Underwater Gravity-Aided Inertial Navigation. 2020 Chinese Automation Congress (CAC), pp. 6250–6253.

Wang, D., Xu, X., Yao, Y., Zhang, T., Zhu, Y., 2019. A novel SINS/DVL tightly integrated navigation method for complex environment. IEEE Trans. Instrum. Meas. https://doi.org/10.1109/TIM.2019.2955187.

Wang, J., Zhang, T., Jin, B., Zhu, Y., Tong, J., 2020. Student's t-based robust kalman filter for a SINS/USBL integration navigation strategy. IEEE Sensor. J. 20 (10), 5540–5553. https://doi.org/10.1109/JSEN.2020.2970766.

Yao, Y., Xu, X., Hou, L., Deng, K., Xu, X., 2020. A simple and precise correction method for DVL measurements under the dynamic environment. IEEE Trans. Veh. Technol. 69, 10750–10758. https://doi.org/10.1109/TVT.2020.3008755.

Yao, Y., Xu, X., Li, Y., Zhang, T., 2019. A Hybrid IMM based INS/DVL integration solution for underwater vehicles[J]. IEEE transactions on vehicular technology. IEEE Trans. Veh. Technol. 68 (6), 5459–5470. https://doi.org/10.1109/TVT.2019.2910397.

Zhang, J., Zhang, T., Shin, H.-S., Wang, J., Zhang, C., 2020. Geomagnetic gradient-assisted evolutionary algorithm for long-range underwater navigation. IEEE Trans. Instrum. Meas. 70 https://doi.org/10.1109/TIM.2020.3034966.

Zhao, G., 2014. Calibration Technique of Optical Gyro SINS. Surveying and Mapping Press.

Zhao, L.-Y., Liu, X.-J., Wang, L., Zhu, Y.-H., Liu, X.-X., 2016. A pretreatment method for the velocity of DVL based on the motion constraint for the integrated SINS/DVL. Appl. Sci. 6 (3) https://doi.org/10.3390/app6030079.

Zhao, S., Zheng, W., Li, Z., Xu, A., Zhu, H., 2021. Improving matching accuracy of underwater gravity matching navigation based on iterative optimal annulus point method with a novel grid topology. Rem. Sens. 13 (22) https://doi.org/10.3390/rs13224616.